

Research Article

An Analytical Model for Bandwidth Enhancement of Air-Coupled Unsealed Helmholtz Structural CMUTs

Xin Liu ^{1,2}, Yuanyu Yu,^{1,2,3} Jiujiang Wang,^{1,2} Sio Hang Pun ¹,
Mang I Vai,^{1,2} and Peng Un Mak ^{2,4}

¹State Key Laboratory of Analog and Mixed-Signal VLSI, University of Macau, 999078, Macau, China

²Department of Electrical and Computer Engineering, Faculty of Science and Technology, University of Macau, 999078, Macau, China

³School of Information Engineering, Lingnan Normal University, Zhanjiang 524048, China

⁴On Leave to Acoustic Wave Physics Group, Department of Chemical Engineering and Biotechnology, University of Cambridge, Cambridge, CB3 0AS, UK

Correspondence should be addressed to Peng Un Mak; fstpum@um.edu.mo

Received 27 December 2018; Revised 6 March 2019; Accepted 27 March 2019; Published 17 April 2019

Academic Editor: Chengkuo Lee

Copyright © 2019 Xin Liu et al. This is an open access article distributed under the Creative Commons Attribution License, which permits unrestricted use, distribution, and reproduction in any medium, provided the original work is properly cited.

Capacitive micromachined ultrasonic transducers (CMUTs) were reported to own high potential in air-coupled ultrasonic applications such as noncontact nondestructive examination and gas flow measurement. The unsealed CMUTs which utilized the squeeze film effect were reported to overcome the narrow output pressure bandwidth of the conventional sealed CMUTs in air operation. This kind of unsealed CMUTs can also be regarded as Helmholtz resonators. In this work, we present the air-coupled unsealed Helmholtz structural CMUTs which utilize both the squeeze film effect and the Helmholtz resonant effect to enhance the output pressure bandwidth. Based on the mechanism of vibration coupling between membrane and air pistons in membrane holes, we propose an analytical model to aid the design process of this kind of CMUTs. We also use finite element method (FEM) to investigate this kind of CMUTs for our analytical model validation. The FEM results show that the significant bandwidth enhancement can be achieved when the Helmholtz resonant frequency is designed close to the fundamental resonant frequency of the CMUT membrane. Compared with the conventional sealed CMUT cell, the 4-hole unsealed Helmholtz structural CMUT cell improves both the 3-dB fractional bandwidth and SPL-bandwidth product around 35 times. Furthermore, it is found that, with more holes under the same hole area ratio or with a smaller ratio of the cavity height to the viscous boundary layer thickness, the Helmholtz resonant effect becomes weaker and thus the output pressure bandwidth decreases.

1. Introduction

Capacitive micromachined ultrasonic transducers (CMUTs) were invented as an alternative to conventional piezoelectric ultrasonic transducers in early 1990s. Compared with the piezoelectric ultrasonic transducers, CMUTs have many advantages such as they are suitable for batch production and can be easily integrated with modern electronics. Conventional piezoelectric ultrasonic transducers typically require matching layers to compensate the acoustic impedance mismatch between piezoelectric materials and surrounding gaseous or liquid media. CMUTs feature a better impedance matching with gaseous and liquid media, and therefore they can transmit/receive ultrasound more efficiently into gas and liquid without the matching layer [1].

In many ultrasonic applications, the transducers were used in immersion [2, 3]. However, in some applications, some objects cannot contact with liquid couplants, such as paper products and electronic products [4]. Also there are many other air-borne ultrasonic applications such as air-coupled ultrasonic imaging [4], ultrasonic distance measurement [5], anthropometrical measurement of scoliosis [6], and gas flow measurement [7]. CMUTs ideally are suited for air-coupled applications because of their good acoustic impedance matching with air.

For air-coupled ultrasonic applications, transducers with wide bandwidth have sharp ultrasonic pulses and short decay time of the vibration amplitude, thus providing high resolution and a small “dead zone” where objects cannot be detected [8]. Wide bandwidth air-coupled transducers are

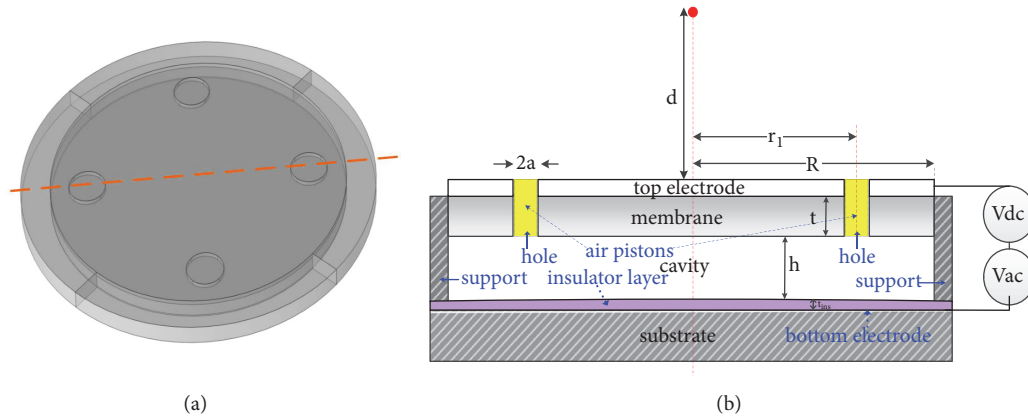


FIGURE 1: (a) A 4-hole unsealed circular CMUT cell with Helmholtz resonator structure. (b) Cross-sectional diagram of this cell along dashed line of (a).

needed for applications such as echo profile evaluation and distance measurement with high resolution [8]. However, the conventional vacuum sealed air-coupled CMUTs still own a narrow bandwidth. For instance, for the CMUT array with only one cell radius, the 6-dB fractional bandwidth is about 1% [9]. To overcome this, unsealed CMUTs were proposed to achieve wider bandwidth by utilizing the squeeze film effects [10–13]. For unsealed CMUTs, the vented cavity not only introduces the squeeze film effects, but also constructs a Helmholtz resonator with the vented holes. The Helmholtz resonator comprised a cavity with an opening denoted as “neck”. When an excitation with a specific frequency range is applied, a volume of air in the neck would vibrate due to the elasticity of the air inside the cavity and thus radiates sound waves into surroundings. This is called Helmholtz resonant effect [14]. The Helmholtz resonant effect can also exert an influence on the device performance; this phenomenon was reported, but there was a lack of analytical explanation in [11]. In [15], the Helmholtz resonant effect was used to enlarge the bandwidth of the CMUT’s output, but, in its FEM simulation, the squeeze film damping was neglected. Actually, with proper adjustment of volume ratio between vented hole and cavity, the performance of the device would be benefited by the vibration coupling between the air pistons vibration system of Helmholtz resonator and the membrane vibration system of CMUT cell. This vibration coupling was widely used to enhance the low frequency response of musical instrument such as acoustic guitar [16] and vented-box loudspeaker systems [17].

In this paper, we present an air-coupled unsealed CMUT cell with Helmholtz resonant cavity, which utilizes both the squeeze film effect and Helmholtz resonant effect to enhance the output pressure bandwidth of the device. For convenience, we hereafter call it as Helmholtz structural CMUT. We propose an analytical model to explain the vibration coupling working mechanism of this kind of CMUT and aid the design process of this kind of CMUT. In order to validate this analytical model and provide deeper investigation on this kind of Helmholtz structural CMUT, the FEM model is built with COMSOL Multiphysics version 5.2a (COMSOL Inc.,

Stockholm, Sweden) to simulate three cases of 4-hole CMUTs with different hole radii.

2. Methodologies

Figure 1(a) shows an air-coupled unsealed Helmholtz structural CMUT cell with 4 holes in its membrane, the cross-sectional illustration of this CMUT cell along the red dashed line in (a) is shown in Figure 1(b). Major components of this CMUT cell are a circular membrane with radius R and thickness t , a cavity with height h , holes with radius a , the thin metal layer as full top electrode, and one insulator layer with thickness t_{ins} to avoid short circuit between electrodes. The bottom electrode is located between the insulator layer and the substrate. The rim of the membrane is clamped by support. Using Helmholtz resonant effect and squeeze film effect to enhance bandwidth, several circular holes need to be punched through the membrane. These holes and the cavity form a Helmholtz resonator. If a DC voltage is applied between top and bottom electrodes, the membrane will be activated by the electrostatic force induced by the voltage and the restoring spring force due to the membrane’s stiffness. When these two forces are equal, the membrane will reach an equilibrium position. Then when a small amplitude AC voltage is superimposed, the unbalance of these two forces will be caused by the small perturbation of the electrostatic force, which leads to the membrane’s vibration. The membrane’s vibration will drive the air pistons in the holes to vibrate due to the elastic property of the air inside the cavity. The vibration of the air pistons will also induce a pressure change in the cavity, which leads to a force acted on the membrane. Therefore, the membrane’s vibration and the air pistons’ vibration interact with each other. During the operation of this air-coupled unsealed Helmholtz structural CMUT cell, the ultrasonic wave will be generated by both vibrations of the membrane and the air pistons.

2.1. Lumped-Parameter Analytical Model. As Figure 2 shows, inspired by the simple model of acoustic guitar [16], the Helmholtz structural CMUT cell can be simplified as a Helmholtz resonator with a movable top plate. The Helmholtz

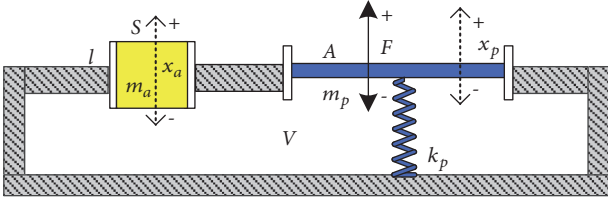


FIGURE 2: Simplified model of Helmholtz structural CMUT cell.

resonator is formed from the cavity of CMUT cell with volume V and an equivalent air piston with mass m_a and top surface area S , where the top surface area S is the sum of top surface areas of all small holes. And we can simplify the membrane as a movable top plate with mass m_p , top surface area A , and stiffness k_p .

Then referencing from [16], we can develop a lumped-parameter analytical model of the air-coupled unsealed Helmholtz structural CMUT cell as follows.

When the DC and AC bias voltages are superimposed, the top plate vibrates as a harmonic oscillator and drives the equivalent air piston to vibrate due to the elastic property of air cushion in the cavity. We assume that the deflected shape of the top plate can be neglected and the uniform displacement of the top plate is denoted as x_p . The uniform displacement of the equivalent air piston is taken as x_a . Then we take outward movement as positive; the volume change of the cavity is

$$\Delta V = Ax_p + Sx_a \quad (1)$$

Thus the pressure change as adiabatic compression in cavity is

$$\Delta p = -\mu\Delta V \quad (2)$$

where $\mu=c^2\rho/V$, c is sound velocity in air, and ρ is the density of air. The forces acted on plate and equivalent air piston due to the pressure change can be represented by $A\Delta p$ and $S\Delta p$, and the equations of the vibrations of the top plate and the equivalent air piston can be written as

$$m_p \frac{d^2 x_p}{dt^2} = F - R_p \frac{dx_p}{dt} - (k_p + \mu A^2) x_p - \mu S A x_a \quad (3a)$$

$$m_a \frac{d^2 x_a}{dt^2} = -R_a \frac{dx_a}{dt} - \mu S^2 x_a - \mu S A x_p \quad (3b)$$

where F is the driving force of top plate, R_a and R_p are resistances to movement of the top plate and the equivalent air piston, respectively. From (3a) and (3b), we can find that the top plate's vibration and the equivalent air piston's vibration are coupled, because they both depend on x_a and x_p . Namely, the vibration of one of them can have effect on the other.

Uncoupled Helmholtz resonator and uncoupled top plate: firstly, if we set $S=0$ in (3a) and $x_p=0$ in (3b), we can get the equations which describe the vibrations of the uncoupled top plate and uncoupled Helmholtz resonator, respectively.

$$m_p \frac{d^2 x_p}{dt^2} = F - R_p \frac{dx_p}{dt} - (k_p + \mu A^2) x_p \quad (4a)$$

$$m_a \frac{d^2 x_a}{dt^2} = -R_a \frac{dx_a}{dt} - \mu S^2 x_a \quad (4b)$$

From (4a), we can get the resonant frequency of the uncoupled top plate as

$$\omega_p = \sqrt{\frac{(k_p + \mu A^2)}{m_p}} \quad (5)$$

Referencing from [18], this frequency can be calculated more accurately as the fundamental resonant frequency of a clamped circular membrane as

$$\omega_p = 2\pi f_p = 2\pi \cdot 0.47 \frac{t}{R^2} \sqrt{\frac{Y}{[\rho_m (1 - \sigma^2)]}} \quad (6)$$

where ρ_m , σ , and Y are membrane material's density, Poisson's ratio and Young's modulus, respectively. From (4b), the resonant frequency of an uncoupled Helmholtz resonator can be solved as

$$\omega_h = 2\pi f_h = \sqrt{\frac{\mu S^2}{m_a}} \quad (7)$$

We substitute $\mu=c^2\rho/V$, $m_a=Sl\rho$ into (7), and we can get

$$\omega_h = c \sqrt{\frac{S}{Vl}} \quad (8)$$

According to [19], the length of the Helmholtz resonator's neck l should take an effective value $l_{eff}=l+\delta$ for better estimation; thus,

$$\omega_h = c \sqrt{\frac{S}{V(l+\delta)}} \quad (9)$$

where δ is the end correction. Referencing from [19], the end correction δ should take the sum of the interior correction δ_i and the exterior correction δ_e as follows:

$$\delta = \delta_i + \delta_e = 0.48\sqrt{S} \left(1 - \frac{1.25\sqrt{n_{hole}a}}{R} \right) + 0.48\sqrt{S} \quad (10)$$

where n_{hole} is the number of holes in the membrane of the CMUT cell.

Coupled Helmholtz resonator and top plate: now, we focus on the coupled vibration system, assuming in harmonic oscillation state, and we solve (3a) and (3b) in frequency domain, by writing in phasor format $x_p = X_p e^{i\omega t}$, $x_a = X_a e^{i\omega t}$, $F = F_0 e^{i\omega t}$, the amplitude of top plate's velocity $U_p = i\omega X_p$, and the amplitude of equivalent air piston's velocity $U_a = i\omega X_a$. Similar to [16], we can get

$$U_p = \frac{i\omega F_0 [(\omega_h^2 - \omega^2) + i\omega\gamma_a]}{m_p D} \quad (11a)$$

$$U_a = \frac{-i\omega F_0 A \omega_h^2}{m_p S D} \quad (11b)$$

where

$$D = (\omega_p^2 - \omega^2 + i\omega\gamma_p)(\omega_h^2 - \omega^2 + i\omega\gamma_a) - \omega_{ph}^4 \quad (12)$$

$$\gamma_a = \frac{R_a}{m_a},$$

$$\gamma_p = \frac{R_p}{m_p},$$

$$\omega_{ph}^4 = \omega_h^2 \omega_a^2,$$

$$\omega_a^2 = \frac{\mu A^2}{m_p} \quad (13)$$

ω_p and ω_h are the resonant frequencies of uncoupled top plate and uncoupled Helmholtz resonator, respectively.

From (11a) and (11b), the coupled vibration system shown in Figure 2 resonates while the moduli of U_a and U_p arrive maximum ($D=0$). If we neglect the damping terms of $i\omega\gamma_a$ and $i\omega\gamma_p$ in (12), then this coupled vibration system's resonant frequencies can be solved as

$$\omega_{\pm}^2 = \frac{\omega_p^2 + \omega_h^2}{2} \pm \frac{\sqrt{(\omega_p^2 - \omega_h^2)^2 + 4\omega_{ph}^4}}{2} \quad (14)$$

As shown in (6) and (9), for the uncoupled top plate and the uncoupled Helmholtz resonator, each of them only has one resonant frequency. From (14) we can see that, unlike the uncoupled situation, both the top plate and the equivalent air piston have two resonant frequencies in the coupled vibration system.

For an air-coupled unsealed Helmholtz structural CMUT cell, when calculating ω_h by (9), the length of the neck l is equal to the membrane's thickness t . And the lumped parameters are calculated as follows:

$$S = n_{hole} \pi a^2 \quad (15)$$

$$A = \pi R^2 - S \quad (16)$$

$$V = \pi R^2 h \quad (17)$$

$$m_p = 1.8 A t \rho_m + m_{rp} \quad (18)$$

$$m_a = S t \rho + m_{ra} \quad (19)$$

where the factor 1.8 in (18) is from [20], m_{rp} is the acoustic radiation mass of the plate, and m_{ra} in (19) is the acoustic radiation mass of the equivalent air piston. Referenced from [21, 22], the CMUT cell should be considered as a clamped plate source located on an infinite baffle, and the acoustic radiation mass of the plate is

$$m_{rp} = -\frac{\rho c A}{\omega} \left[\frac{20F_2(2(\omega/c)\sqrt{A/\pi})}{((\omega/c)\sqrt{A/\pi})^9} \right], \quad (20)$$

$$F_2(x) = -(x^4 - 91x^2 + 504)H_1(x) - 14x(x^2 - 18)H_0(x) + \frac{14x^4}{15\pi} - \frac{168x^2}{\pi}$$

where $H_n(x)$ is the n th order Struve function. The equivalent air piston is considered as a baffled piston source; the radiation mass of the equivalent air piston is [14]

$$m_{ra} = n_{hole} \frac{\rho c (\pi a^2)}{\omega} \left[\frac{2H_1(2(\omega/c)a)}{(2(\omega/c)a)} \right] \quad (21)$$

In the simplification in Figure 2, the driving force F is a harmonic force; hence, we take F as the harmonic electrostatic force, according to [1],

$$F_0 = |F_{ac}| = \frac{\epsilon_0 A V_{dc} V_{ac}}{h^2} \quad (22)$$

where V_{dc} , V_{ac} are DC voltage and AC voltage applied to the cell, and ϵ_0 is the dielectric permittivity of air.

The squeeze film effect includes squeeze film stiffening effect and squeeze film damping effect. The proportion of the stiffening effect and damping effect is determined by the squeeze number [20]

$$\sigma_{squeeze} = \frac{12\mu_{air}\omega R^2}{P_a h^2} \quad (23)$$

where μ_{air} is the dynamic viscosity of air, P_a is the ambient pressure, and ω is the plate's vibrating angular frequency. For the air-coupled unsealed CMUT with perforated membrane, the squeeze damping effect dominates the squeeze film effect because of the small squeeze number, and the squeeze stiffening effect can be neglected [20, 23]. From [20], the squeeze damping can be represented by the lump resistance as

$$R_{squeeze} = \frac{3\pi\mu_{air}R^4\kappa(\beta)}{2h^3 n_{hole}} \quad (24)$$

where

$$\kappa(\beta) = 4\beta^2 - \beta^4 - 4\ln(\beta) - 3 \quad (25)$$

$$\beta = \frac{a}{(1.05r_1/\sqrt{2})} \quad (26)$$

where r_1 represents the distance between center of hole and center of membrane and n_{hole} is the total number of holes.

For the plate, although there are other damping mechanisms, the squeeze film damping is the most noticeable once it is presented in MEMS devices [23]. In addition, CMUT is an acoustic device; the loss of acoustic radiation cannot be ignored [10]. According to [21, 22], the resistance of the acoustic radiation of the clamped plate is

$$R_{rad_plate} = \rho c A \left[1 - \frac{20F_1(2(\omega/c)\sqrt{A/\pi})}{((\omega/c)\sqrt{A/\pi})^9} \right], \quad (27)$$

$$F_1(x) = (x^4 - 91x^2 + 504)J_1(x) + 14x(x^2 - 18)J_0(x) - \frac{x^5}{16} - \frac{x^7}{768}$$

where $J_n(x)$ is the Bessel function of the first kind of order n . Thus, the damping resistance of the top plate R_p is

$$R_p = R_{squeeze} + R_{rad_plate} \quad (28)$$

where $R_{squeeze}$ is calculated as in (24) to (26). R_{rad_plate} is calculated as in (27).

For the equivalent air piston, not only the acoustic radiation damping but also the viscous damping needs to be considered. When the air pistons vibrate, due to the viscosity of the air, they are damped by the viscous force at the side walls of the holes. From [24], the resistance of viscous boundary layer per unit area can be expressed as

$$R_{visc} = \sqrt{\frac{\rho\mu_{air}\omega}{2}} \quad (29)$$

When calculating the viscous damping of the equivalent air piston, the area of viscous boundary layer is taken as the area of the side walls of the holes and a viscous end correction [19]. The resistance of acoustic radiation $R_{rad_air\ piston}$ is calculated as the baffled piston source [14].

$$R_{rad_air\ piston} = n_{hole}\rho c \left(\pi a^2 \right) \left(1 - \frac{2J_1(2\omega a/c)}{2\omega a/c} \right) \quad (30)$$

Thus, the damping resistance of the equivalent air piston is

$$R_a = n_{hole} \left(2\pi a t + 4\pi a^2 \right) R_{visc} + R_{rad_air\ piston} \quad (31)$$

After getting U_a and U_p , the complex amplitude of total volume velocity U can be written as

$$U = AU_p + SU_a \quad (32)$$

From [21, 25], if we consider a CMUT cell as a clamped edge radiator source, the complex amplitude of sound pressure of the point at distance d in the far field above the center of the membrane can be calculated as

$$p = \frac{i\omega\rho U}{2\pi d} \quad (33)$$

then the sound pressure level (SPL) at this point can be calculated.

2.2. Finite Element Method Model. In order to investigate the air-coupled unsealed Helmholtz structural CMUTs and validate the analytical model, we have developed the finite element method (FEM) model to simulate the device. Unsealed CMUTs would induce squeeze film effect; usually the squeeze film effect in MEMS devices is described by nonlinear compressible Reynolds equation, which is simplified from the continuity equation and the Navier-Stokes equation when the modified Reynolds number satisfies [13, 20]

$$Re_{modified} = \frac{\omega\rho h^2}{\mu_{air}} \ll 1 \quad (34)$$

This condition is not effective for CMUTs which have slightly higher gaps or higher operating frequencies. Thus, we need

to start with the continuity equation and the Navier-Stokes equation to model the squeeze film effect in our unsealed Helmholtz structural CMUTs [13].

The commercial software COMSOL Multiphysics version 5.2a is used to build our FEM model. The Electromechanical (*emi*) module and Thermoviscous Acoustics, Frequency Domain (*ta*) module are used in our FEM model of a CMUT cell. The governing equations of *ta* include the Navier-Stokes equation, the continuity equation, and the energy equation formulated using the Fourier heat law [26]. Thus, the squeeze film effect is included and the thermal loss is also taken into account.

We use four symmetric distributed holes here to avoid the damage of the center part of membrane which makes main contribution to membrane's vibration. Table 1 lists the material properties in simulation. The 3D model of a quarter of a CMUT cell in octant spherical air domain is built, as shown in Figures 3(a) and 3(b). A "perfectly matched layer (PML)" is used to eliminate the acoustic reflection and to simulate an infinite spread medium. In *emi* module, for the "domain selection", it includes all domains. The membrane, the insulator layer, and the support are selected as "linear elastic dielectric". The rim of the membrane, the support, and the insulator layer are applied with "fixed constraint" boundary condition. The substrate can be ignored because of the fixed insulator layer. For simplification in FEM, the top and bottom electrodes can be regarded as infinitely thin [27]; thus, we directly use the membrane's top surface as the top electrode, and the bottom electrode is located underneath the insulator layer. A constant DC bias voltage and a harmonic AC voltage (amplitude as 1% of DC voltage) are applied on the top surface of membrane by the "terminal" with "harmonic perturbation" conditions, and the bottom surface of insulator layer is set as "ground". The "symmetry" is applied on the vertical sections of the membrane, insulator layer, and support. Other boundary conditions keep the default setting in COMSOL. In *ta* module, for the "domain selection", only domains filled with air (cavity, holes, spherical air domain, PML) are selected. To couple two modules, "velocity" and "isothermal" boundary conditions are applied in *ta* on the top surface of membrane and inner wall of cavity and of hole, which are interfaces between *ta* and *emi* [26]. The "velocity" in *ta* is prescribed as in *emi*. This coupling setting is a two-way coupling, which means when the membrane vibrates to generate sound waves in medium, a reaction force would be added to the membrane [28]. Thus we do not need to add other coupling condition in *emi* module. The "symmetry" boundary condition is applied on the vertical sections of cavity and the vertical sections of octant spherical air and PML. Other boundary conditions keep the default setting in COMSOL. In the mesh setup, the mesh size should be sufficiently small to resolve the wavelength by at least 5-6 elements per wavelength [29], and the maximum element size of the acoustic medium is set as one-sixth of wavelength of operating frequency. Also the "boundary layers mesh" is needed at the inner walls of both cavity and holes; the thickness of "boundary layers mesh" is equal to the viscous boundary layer thickness under fundamental resonant frequency of CMUTs membrane [26]. The meshing details of

TABLE 1: Material properties used in COMSOL (*: the factor 0.6 is from [30]; others are the preset values/functions in COMSOL).

Parameter	Value/Preset function in COMSOL
<i>Air: (used in cavity, holes, spherical air domain, PML)</i>	
Relative permittivity	1
Dynamic viscosity μ_{air} [Pa.s]	eta(T[1/K])
Heat capacity at constant pressure C_p [J/(kg.K)]	Cp(T[1/K])
Density ρ_{air} [kg/m ³]	rho(pA[1/Pa],T[1/K])
Thermal conductivity K [W/(m.K)]	k(T[1/K])
*Bulk viscosity μ_b [Pa.s]	0.6*eta(T[1/K])
Typical Wave Speed for PML [m/s]	343
<i>Si: (used in membrane, support beam)</i>	
Young's modulus Y [GPa]	170
Poisson ratio σ	0.28
Density ρ_{Si} [kg/m ³]	2329
Relative permittivity	11.7
<i>SiO₂: (used in insulator layer)</i>	
Young's modulus [GPa]	70
Poisson ratio	0.17
Density [kg/m ³]	2200
Relative permittivity	4.2

vertical section of the cell are shown in Figure 3(c), where the “boundary layers meshes” are highlighted. The “prestressed analysis” is applied in calculating the average pressure over different frequencies. Firstly, a stationary study is used to calculate the membrane deflection under a certain DC bias voltage. Then an AC voltage is biased on the membrane using harmonic analysis over a frequency range. The pressure is calculated by averaging the pressure between the membrane and the air medium.

In order to make a comparison between the unsealed Helmholtz structural CMUTs and the conventional vacuum sealed CMUTs, we also build an FEM model for the latter. The model building process of the conventional cell is slightly different from the unsealed Helmholtz structural CMUT cell. The solid-air interfaces for the conventional cell only contain the top surface of the membrane; thus, the “velocity” and “isothermal” are only added on the membrane’s top surface. The cavity is vacuum; thus, for a conventional cell, we do not take the acoustic field of the cavity into *ta* module’s calculation. Also, the “boundary layers mesh” is not needed for the vacuum cavity.

3. Results

3.1. FEM Results. We take three (Standard, Double, and Half) cases in FEM simulation; Table 2 shows the parameters of physical structural dimension of the CMUT cell used. The main target of this paper is to demonstrate synergy properties of both the squeeze film effect and the Helmholtz resonant effect in CMUTs. In order to fulfill this, we set

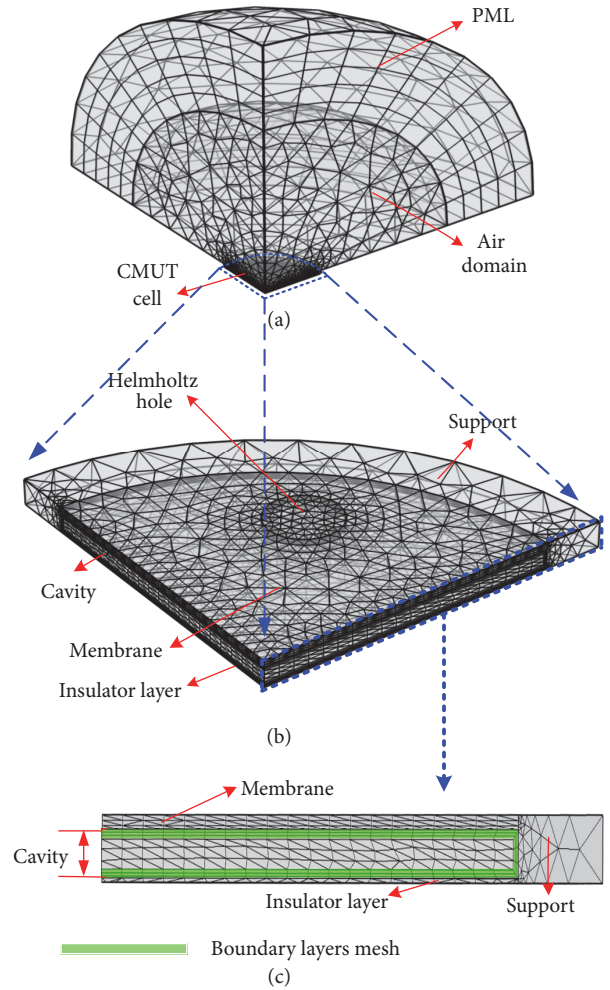


FIGURE 3: A 3D model in COMSOL: (a) a quarter of a CMUT cell and spherical air domain; (b) details of the unsealed Helmholtz structural CMUT cell; (c) meshing details of the vertical section of (b).

the corresponding parameters and they turn out to be a bit large for Standard case. In the Standard case, the radius R and thickness t of membrane are referenced from [12] as a representative one. The cavity height h is designed to achieve a proper $h/2\sigma_{visc}$ ratio to generate the obvious Helmholtz effect, where σ_{visc} is the thickness of the viscous boundary layer, as we will explain in the discussion section. For air-coupled CMUTs, designs and fabrications with such large cell dimensions can be found in [31, 32]. The fabrication method of the vented holes can be found in [12, 13]. In the Double case, the physical dimension parameters are 2 times of the Standard case. In the frequency response, the vibration coupling characteristic of two resonant peaks is more obvious with such large dimension cells, because the proportion of thermal viscous loss energy to the total energy gets lower when the cell dimension increases from Half case to Double case, as we shall show in discussion section. The results of the Double case with obvious characteristic are helpful to clearly

TABLE 2: Parameters of CMUT cells in our design.

Parameters	Double	Standard	Half
R membrane radius [μm]	1000	500	250
h cavity height [μm]	60	30	15
t membrane thickness [μm]	20	10	5
a_{ini} initial hole radius [μm]	110	55	27.5
a hole radius [μm]	40, 80, 120, 160, 200	20, 40, 60, 80, 100	10, 20, 30, 40, 50
t_{ins} insulator layer thickness [μm]	6	3	1.5
r_1 hole position [μm]	750	375	187.5
n_{hole} holes number	4	4	4
V_{dc} DC voltage [V]	6720	3360	1680

investigate the working mechanism of Helmholtz structural CMUT. In the Half case, the physical dimension parameters are taken as half of the Standard case. As we shall show in discussion section, this case is to investigate influence factor of the Helmholtz effect.

For hole radius, we use (6) to calculate f_p ; let $f_h = f_p$, then use (9), (10), and (15) to solve an initial hole radius a_{ini} of each hole as

$$a_{ini} = \frac{0.96\sqrt{n_{hole}\pi}q_a + \sqrt{0.96^2n_{hole}\pi q_a^2 - 4(1+q_aq_b)(-q_at)}}{2(1+q_aq_b)} \quad (35)$$

where

$$q_a = \left(\frac{2\pi f_p}{c}\right)^2 \left(\frac{V}{n_{hole}\pi}\right) \quad (36)$$

$$q_b = \frac{0.6\sqrt{\pi}n_{hole}}{R} \quad (37)$$

Then choose hole radius around a_{ini} . In each case in Table 2, compared with the no-hole cell, the collapse voltage of the CMUTs with 4 holes decreases a little. For simplicity, the DC voltage is taken as about 70% of the collapse voltage of the no-hole cell.

Firstly, the Double case is considered to show the vibration coupling working mechanism of the air-coupled unsealed Helmholtz structural CMUTs.

The membrane and air piston's motions are mainly on vertical direction; thus, in COMSOL, we take the amplitude of the membrane's velocity U_p and the amplitude of the air piston's velocity U_a as the z directional average velocity complex amplitude of the membrane's top surface and of the hole's top surface, respectively.

Figure 4 shows magnitudes of U_p and U_a . As shown in Figure 4, for unsealed Helmholtz structural CMUTs with different hole sizes, as mentioned in methodologies section, the magnitudes of U_p and U_a have two resonant frequencies corresponding to $f_- = \omega_-/2\pi$, $f_+ = \omega_+/2\pi$, respectively. It is noticeable that between these two resonant peaks there is a trough, whose corresponding frequency is called the antiresonant frequency. Referring to [16], this antiresonant frequency is equal to the resonant frequency of uncoupled Helmholtz resonator f_h .

The FEM complex amplitude of total volume velocity U is calculated as (32). Figure 5 shows its magnitude $|U|$. Also, $|U|$ of the unsealed Helmholtz structural CMUTs has two resonant frequencies, locating at two sides of the peak of the vacuum sealed cell at fundamental resonant frequency $f_p = 83$ kHz.

Figure 6 illustrates the air pistons' and the membrane's contributions to the magnitudes of total volume velocity $|U|$ of the unsealed Helmholtz structural CMUT cells. Contributions of air pistons and the membrane are represented by the magnitudes $|SU_a|$ and $|AU_p|$, respectively. In order to mark the fundamental resonant frequency f_p , we also add the magnitudes of total volume velocity of the vacuum sealed cell. From Figures 6(a) and 6(b), for the unsealed Helmholtz structural CMUT cells, when $f_h < f_p$, the air pistons make major contribution to the left peak of $|U|$ at f_- , and to the right peak at f_+ while $f_h > f_p$. In simpler terms, for the unsealed Helmholtz structural CMUT cells, the air pistons mainly contribute to the resonant peak whose corresponding frequency is farther from f_p than the other resonant peak.

The CMUTs from the Double case to the Half case have different working frequencies; thus, at the point with same distance from the CMUT cells, the acoustic attenuation differs among cases. In order to fairly compare the output pressure from the Double case to the Half case, the SPL is taken at the top surfaces of membrane and hole. We first take the area average sound pressure of the top surfaces of membrane and hole then calculate the SPL. Figure 7 shows the SPLs over the membrane and hole's top surface. From (33), the sound pressure is proportional to U ; on this account, each curve in Figure 7 has two resonant peaks at resonant frequencies of its corresponding curve in Figure 5. As shown in Figure 7, compared with the sealed one, the SPLs of unsealed Helmholtz structural CMUTs realize the dual-band and extend range of frequency response towards wider frequencies.

Secondly, for the Standard case in Table 2, the FEM results of SPLs are shown in Figure 8. Two resonant frequencies due to the vibration coupling also can be observed for the unsealed cells. As we can see from Figure 8, for SPLs, the bandwidths of unsealed Helmholtz structural CMUT cells are obviously larger than the conventional sealed CMUT cell. However, compared with the sealed cell, the energy loss in the form of squeeze damping loss, viscous loss, and thermal

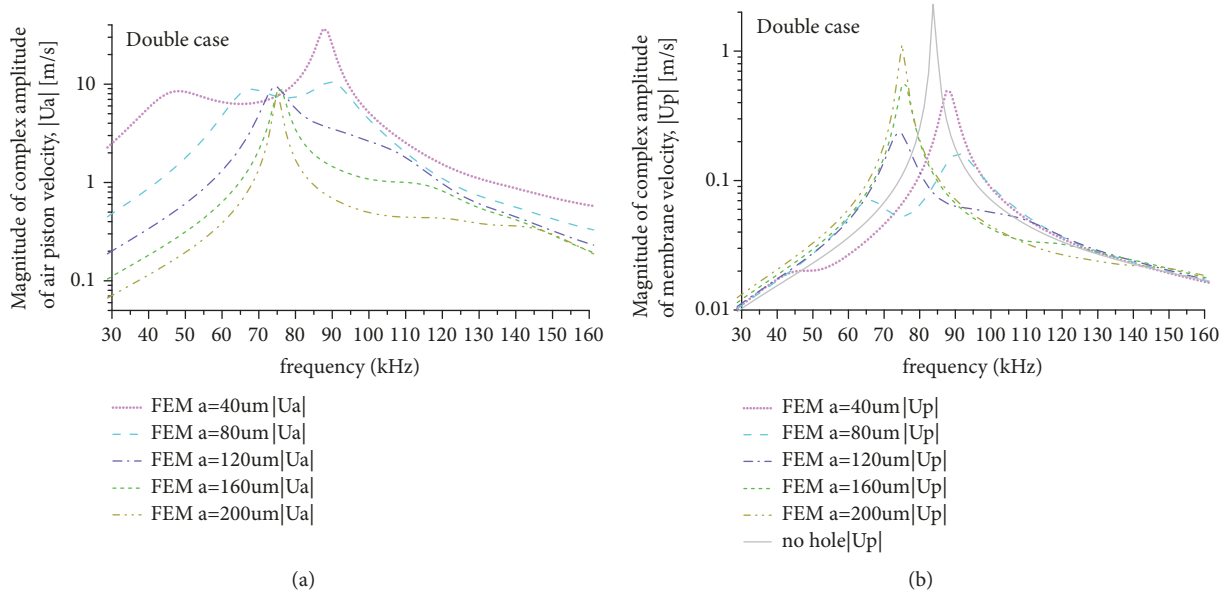


FIGURE 4: FEM results of the Double case: (a) magnitude of complex amplitude of air piston velocity; (b) magnitude of complex amplitude of membrane velocity.

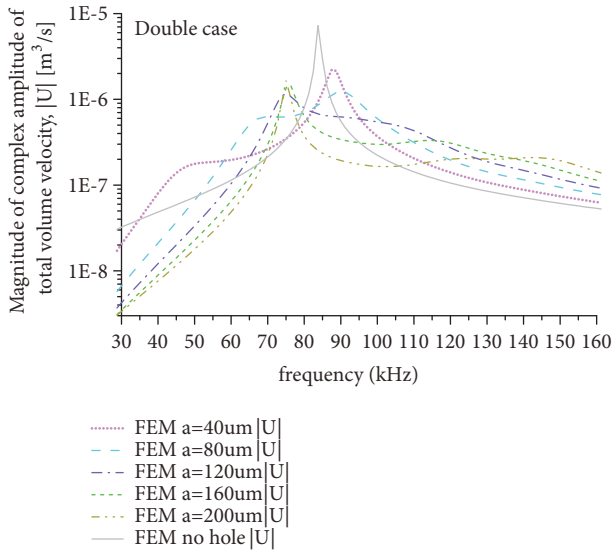


FIGURE 5: FEM results of the Double case: magnitude of complex amplitude of total volume velocity.

loss is introduced in the cavity and holes of the unsealed Helmholtz structural CMUT cell. Under the same V_{dc} and V_{ac} , for the sealed cell, the electrical energy is converted into the acoustic energy, while for the unsealed cell, the electrical energy is converted into the acoustic energy and the energy loss in the cavity and holes. Thus the pressure values of the Helmholtz structural CMUT cells are lower than the sealed one. Referring to [33], we define the SPL-bandwidth product as bandwidth [MHz] \times peak value of SPL [dB]; both bandwidth and pressure values performance of the CMUTs can be reflected by this product. We calculate the 3-dB fractional bandwidth and SPL-bandwidth product

of the CMUT cells in Figure 8; the results are listed in Table 3.

As shown in Table 3, the f_p is calculated from (6) and the f_h is calculated from (9) and (10); when f_h is close to f_p , the unsealed Helmholtz structural CMUT cell with $a = 60\mu\text{m}$ achieves a significant improvement around 35 times of the conventional sealed cell in both 3-dB fractional bandwidth and SPL-bandwidth product. Other unsealed dimensions also have performance enhancement compared with the conventional sealed one. Therefore, compared with the conventional sealed cell, unsealed Helmholtz structural CMUT cells not only enhance the bandwidth of SPL but also keep the pressure value at a reasonable level.

Last, for the Half case in Table 2, the FEM results of the SPLs over the top surfaces of the membrane and hole are shown in Figure 9, and the corresponding 3-dB fractional bandwidth and the SPL-bandwidth product are listed in Table 4. The characteristic of two resonant peaks is not so obvious as the Double case and the Standard case. However, the significant enhancement around 17 times of the conventional sealed cell still is achieved while f_h is close to f_p ($a = 30\mu\text{m}$ cell). Unsealed Helmholtz structural CMUT cells still have a performance enhancement over the conventional sealed CMUT cell.

As shown above in Tables 3 and 4, compared with the conventional sealed CMUT cell, the air-coupled unsealed 4-hole Helmholtz structural CMUT cells achieved the enhancement of both 3-dB fractional bandwidth and SPL-bandwidth product, and the significant enhancement was achieved while f_h is close to f_p .

3.2. Analytical Results Compared with FEM Results. In order to validate our analytical model, we make a comparison between analytical results and FEM results from all cases. For the analytical results, we first use (15) to (22), (28) and (31)

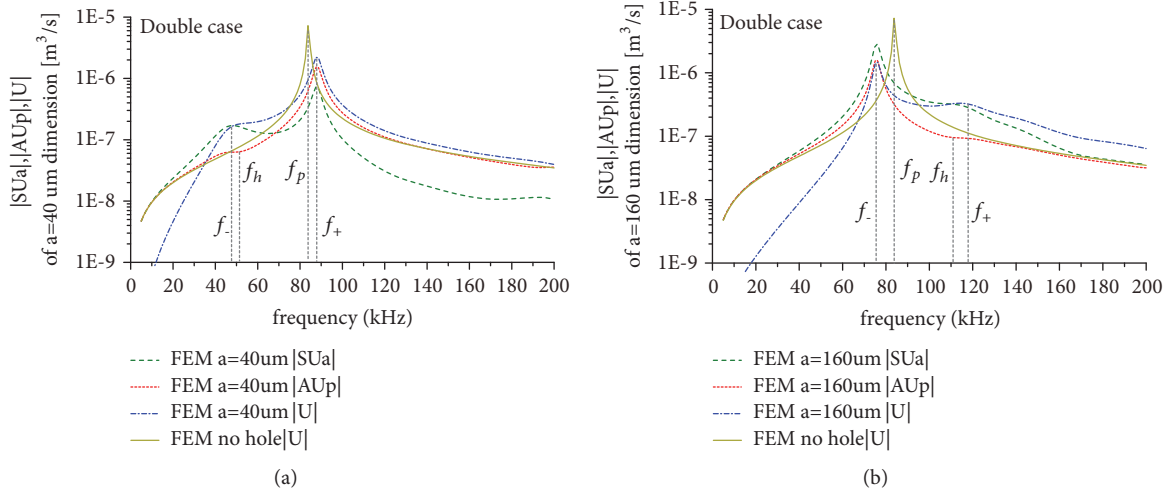


FIGURE 6: FEM results of the Double case: (a) $|SU_a|$, $|AU_p|$, $|U|$ of $a=40\mu\text{m}$ dimension ($f_h < f_p$); (b) $|SU_a|$, $|AU_p|$, $|U|$ of $a=160\mu\text{m}$ dimension ($f_h > f_p$).

TABLE 3: 3-dB fractional bandwidth and SPL-bandwidth product of the Standard case as shown in Figure 8.

Hole radius [μm]	$a=20$	$a=40$	$a=60$	$a=80$	$a=100$	no hole
f_h [kHz]	92.3	138.5	176.5	211.3	244.7	$f_p=167.5$
Separation between f_p and f_h [kHz]	75.2	29	9	43.8	77.2	
3-dB fractional bandwidth	4.8%	11.6%	35.7%	7.3%	3.8%	0.9%
SPL-bandwidth product	1.22	2.88	8.01	1.51	0.77	0.23

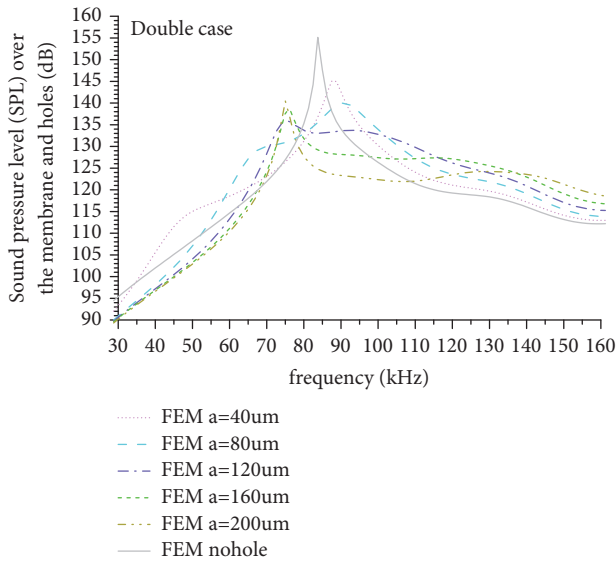


FIGURE 7: FEM results of the Double case: sound pressure level (SPL) over the membrane and hole's top surface (dB).

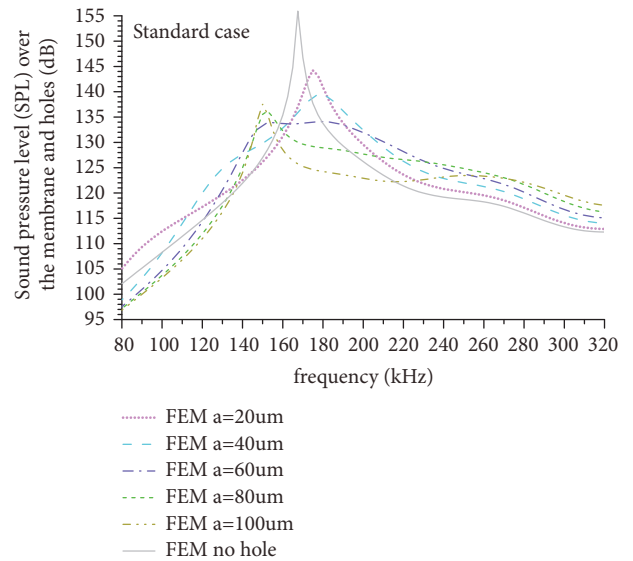


FIGURE 8: FEM results of the Standard case: sound pressure level (SPL) over the membrane and holes (dB).

to calculate values of basic parameters; then, we use (6) to get ω_p , and we use (9) and (10) to get ω_h . After that we use (11a) to (13) to get U_p and U_a , then we substitute back (32) to get U and use (33) to get p at a point above ($d = 3600\mu\text{m}$ in the Double case, $d = 1800\mu\text{m}$ in the Standard case, $d = 900\mu\text{m}$ in the Half case) the center of the membrane. Then

we calculate SPL at this point. In this section, the FEM SPL results also are calculated at the same corresponding point above the center of the membrane. The comparison results are shown in Figure 10.

One point we would like to mention, in (20) and (27), we calculate the acoustic radiation impedance of the CMUT

TABLE 4: 3-dB fractional bandwidth and SPL-bandwidth product of the Half case as shown in Figure 9.

Hole radius [μm]	$a=10$	$a=20$	$a=30$	$a=40$	$a=50$	no hole
f_h [kHz]	184.6	277.1	353.1	422.6	489.6	$f_p=334.9$
Separation between f_p and f_h [kHz]	150.3	57.8	18.2	87.7	154.7	
3-dB fractional bandwidth	5.4%	10.9%	24.0%	14.7%	6.5%	1.3%
SPL-bandwidth product	2.67	5.29	11.06	6.08	2.62	0.67

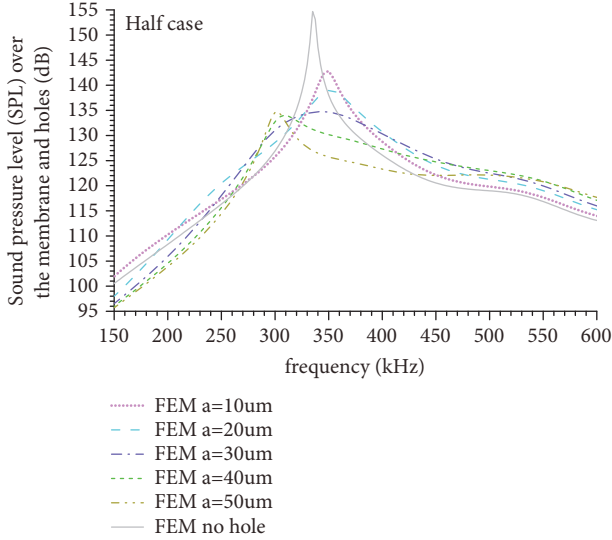


FIGURE 9: FEM results of the Half case: sound pressure level (SPL) over the membrane and holes (dB).

membrane by the formulas of the baffled clamped plate source. From [22], the piston plate radiation and the clamped plate radiation are almost same for $kR_{source} < 1$, where k is the wave number and R_{source} is the source radius. In our design, the value of kR_{source} is small; thus, we can also use baffled piston source to calculate the acoustic radiation impedance of the CMUT membrane; the analytical results are almost same by using these two ways to calculate acoustic radiation impedance of the CMUT membrane.

In order to evaluate the similarity between the analytical SPL results and the FEM SPL results, we calculate the normalized mean square error (NMSE) between our analytical results and FEM results [34].

$$NMSE \text{ value} = 1 - \frac{\|\vec{x}_{ref} - \vec{x}\|^2}{\|\vec{x}_{ref} - \text{mean}(\vec{x}_{ref})\|^2} \quad (38)$$

The NMSE values vary between negative infinity (not fit) and 1 (perfect fit). In each subgraph in Figure 10, we take FEM results and analytical results as \vec{x}_{ref} and \vec{x} , respectively. The calculated NMSE values in Table 5 indicate our analytical results have a good matching with FEM results.

The deviations between analytical results and FEM results could be caused by the simplifications of the analytical model such as negligence of the membrane's deformation and assumption as a plate with uniform displacement. In (22), the analytical driving force is only taken as the harmonic part

TABLE 5: Normalized mean square error (NMSE) values between analytical results and FEM results in Figure 10.

<i>Double case</i>	$a=80\mu\text{m}$	$a=120\mu\text{m}$
NMSE	0.9173	0.9347
<i>Standard case</i>	$a=40\mu\text{m}$	$a=60\mu\text{m}$
NMSE	0.9355	0.9513
<i>Half case</i>	$a=20\mu\text{m}$	$a=30\mu\text{m}$
NMSE	0.9523	0.9689

of the electrical force. In (28) and (31), the loss taken into consideration is only the squeezing, viscous and radiation loss, not including the thermal loss which is included in the FEM model. And in the analytical model we use the equivalent air piston instead of four small air pistons in the holes; thus, the interaction among holes is neglected. Compared with the no-hole cell, the membrane stiffness and the uncoupled natural resonant frequency of the 4-hole CMUT cell decrease. In [15], the natural resonant frequency of the membrane with holes was approximated by the formula of the no-hole membrane. For our design, using (6) of the no-hole membrane to approximate the natural resonant frequency of the 4-hole membrane would not have a significant influence of the analytical results. In the future work, the accurate formula of the natural resonant frequency of the membrane with holes will be investigated.

However, this analytical model gives the explanation of the most significant vibration coupling mechanism of the air-coupled unsealed Helmholtz structural CMUTs and can be used to predict the characteristics such as $|U|$, SPL and f_+ and f_- of this kind of CMUTs during the design process. Figure 11 shows the flow chart on how the analytical model can be used to aid the design of Helmholtz structural CMUTs. In the design phase of Helmholtz structural CMUTs, for the membrane with inputted thickness t and radius R , we firstly select an h value within the interval $[4\sigma_{visc}, h_{max}]$, where the lower limit $4\sigma_{visc}$ is for the obvious Helmholtz resonance, and the consideration of the limitation of DC voltage and maximum allowed gap height is included in h_{max} . Then sweep hole radius a around the calculated initial hole radius a_{ini} to get the point SPL and perform the FEM simulation of the dimension neighbored around the hole radius with significant performance enhancement to search for more accurate fine results. If there is no significant performance enhancement for all of the swept hole radii, then we need to reselect the h value, and sweep hole radius a around the new calculated a_{ini} to find performance enhanced cell dimension.

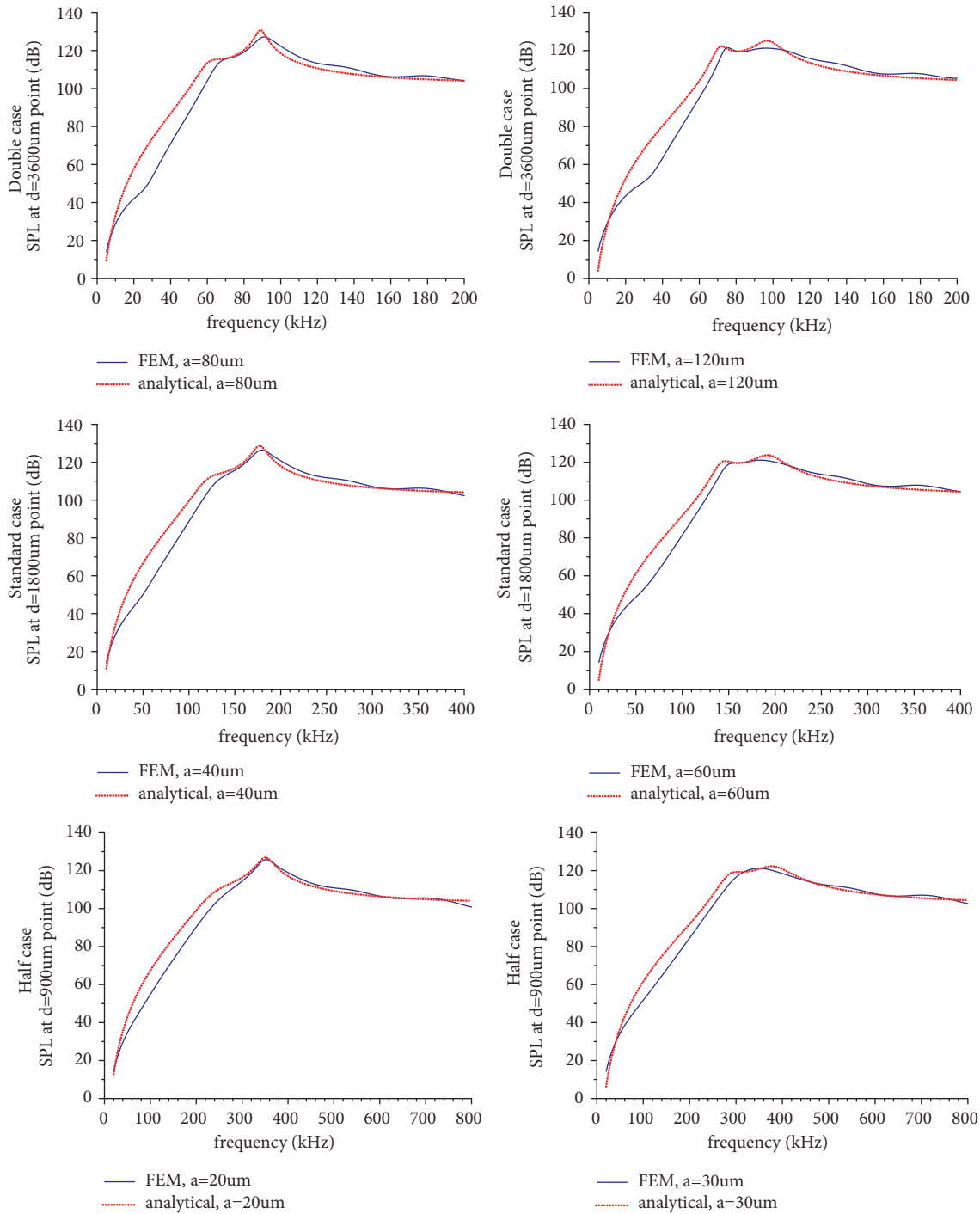


FIGURE 10: Comparison of analytical and FEM results of SPL at a point above the center of the membrane.

If there is no proper h , we need to go back to reinput t and R . Using this design process, the analytical model can help us to initially pick out the cell dimensions with performance enhancement. Then we only need to perform the FEM simulations of these dimensions to check more accurate results. This simplifies the design process and shortens the design period, saving a lot of computation time with our reasonable guesstimates of analytical design procedure.

4. Discussion

4.1. Explanation of the Decreased Phenomenon of the Two Resonant Peaks. In this section, we make a comparison of the FEM results of SPLs from the Double case to the Half case and give an explanation of the decreased phenomenon of the two resonant peaks. As we can see from Figure 8, for the SPL of the unsealed Helmholtz structural CMUT cells in

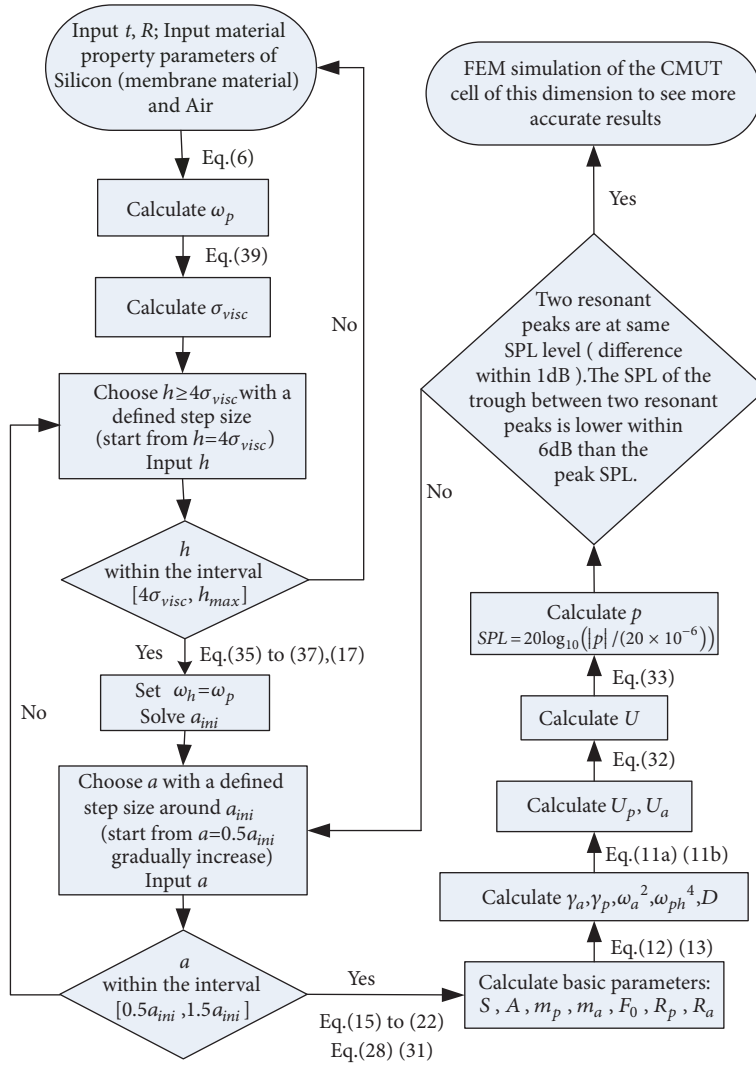


FIGURE 11: The flow chart of using analytical model to aid the design process of Helmholtz structural CMUTs.

the Standard case, the left peaks of cells with $f_h < f_p$ and the right peaks of cells with $f_h > f_p$ are not as evident as the Double case in Figure 7. For the Half case in Figure 9, for the unsealed Helmholtz structural CMUT cells, the peaks majorly contributed by air pistons appear further weakly and even almost disappear. This is due to the thermal viscous loss, which is caused by viscosity and heat conduction.

When sound propagates in structures with small geometric dimensions, the interaction between air and solid boundaries gives rise to the viscous boundary layer and the thermal boundary layer. In these two boundary layers, the loss is much greater than in the free field which is far away from the solid boundaries. The thicknesses of these two boundary layers are calculated as [24]

$$\sigma_{visc} = \sqrt{\frac{2\mu_{air}}{\rho_{air}\omega}} \approx \frac{2.2 \times 10^{-3}}{\sqrt{f}} \quad (39)$$

$$\sigma_{therm} = \sqrt{\frac{2K}{\rho_{air}C_p\omega}} \approx \frac{2.5 \times 10^{-3}}{\sqrt{f}} \quad (40)$$

For viscous boundary layer, as Figure 12 shows, we can regard the flow in the cavity and the holes as shear flow; it can be divided into two parts: the part within σ_{visc} is heavily damped and with great mechanical loss and the other part far from σ_{visc} is free and lossless. As listed in Table 6, the ratio $h/2\sigma_{visc}$ reduces from the Double case to the Half case. Therefore, for the whole flow in the cavity and the holes, the proportion of the part with heavy loss increases and the proportion of the lossless part decreases. That means more portion of the energy is dissipated by the boundary layers, and portion of the energy provided for the air pistons' vibration gets weaker; as a consequence, the peak mostly contributed by air pistons gets weaker. For thermal boundary layer, also the proportion of the total energy to the thermal loss energy can be reflected by the ratio $h/2\sigma_{therm}$. For our designed CMUTs parameters, the thermal loss can be neglected compared with the squeeze film loss and the radiation loss. Thus in our analytical model, we did not take the thermal loss into account.

We have also simulated other two cases whose dimensions are 10 times and 0.1 times of the Standard case in Table 2.

TABLE 6: Ratio of cavity height to $2\sigma_{visc}$, taking f as f_p in (6).

	Double case	Standard case	Half case
$h/2\sigma_{visc}$	3.94	2.79	1.97

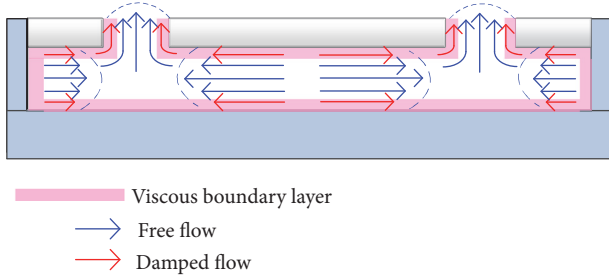
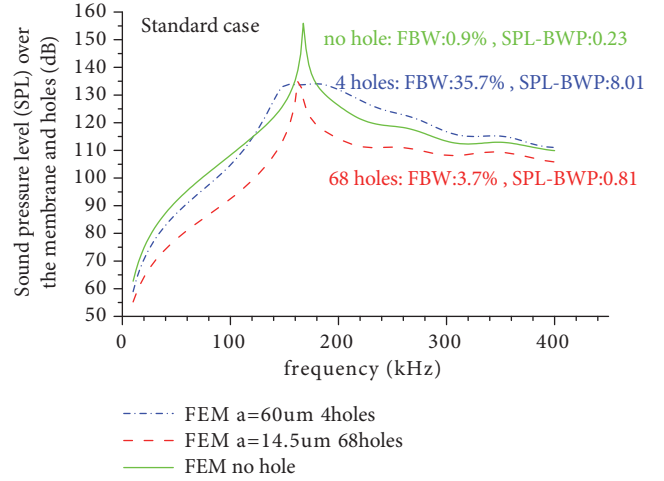
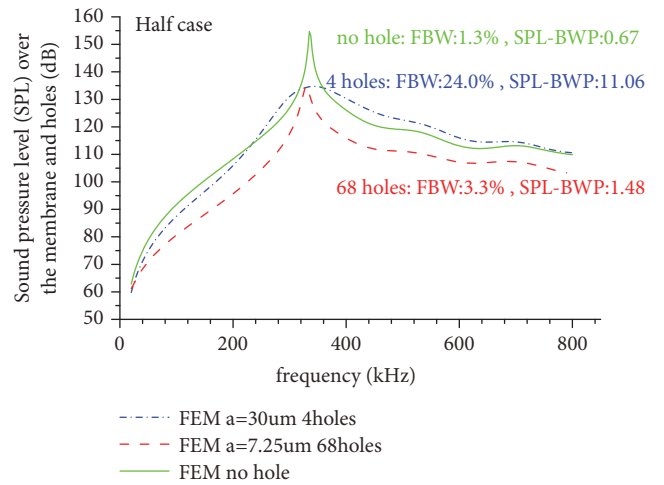


FIGURE 12: Illustration of viscous boundary layer and flow in cavity and holes.

The results are in accordance with our explanation above. For the 10 times case, the two resonant peaks are obvious. But for the 0.1 times case, the Helmholtz resonant effect tends to disappear; only one resonant peak is observed in the SPL frequency response. We also did FEM simulations and analytical analyses for a $R = 650 \mu\text{m}$, $t = 10 \mu\text{m}$, and $h = 30 \mu\text{m}$ 4-hole cell with different hole radii. Compared with the cell in Standard case, the Helmholtz effect gets weaker because of the decreased $h/2\sigma_{visc}$ ratio. Thus when we sweep hole radii from $25 \mu\text{m}$ to $45 \mu\text{m}$ around $a_{ini} = 36 \mu\text{m}$, the two resonant peaks cannot be within 3 dB level and cannot achieve the 3 dB bandwidth improvement like $a = 60 \mu\text{m}$ cell in Figure 8.

4.2. Contribution of Helmholtz Resonant Effect to the Output Enhancement of the 4-Hole Cell. Here we check the bandwidth and SPL-bandwidth product enhancement of the unsealed Helmholtz structural CMUTs is indeed affected by the Helmholtz resonator, although the vibration coupling feature of two resonant peaks is not obvious in Figures 8 and 9. The hole area ratio is defined as the total hole area divided by the total membrane area, i.e., $n_{hole}\pi a^2/\pi R^2$. We simulate an unsealed cell with 68 holes uniformly distributed on the membrane and having the same hole area ratio as the cell ($a=60\mu\text{m}$, 4 holes) with significant enhancement in the Standard case. Other dimension parameters of this 68-hole cell remain the same as the Standard case in Table 2. Thus from (9), (10), and (15), for the 4-hole cell and the 68-hole cell, they have the same value of the uncoupled Helmholtz resonant frequency f_h . The simulation results are shown in Figure 13. We can see from Figure 13, as we explained in Figure 12, in spite of the same f_h , there is more air-solid contact area contributed by holes' side wall in the 68-hole cell. Hence, there are more lossy flows which weaken the vibration of air pistons of Helmholtz resonator. Therefore, the performance of 68-hole CMUT with decreased Helmholtz resonator effect is much less than the 4-hole one's.

We also simulate another 68-hole cell which has the same hole area ratio as the cell ($a=30\mu\text{m}$, 4 holes) with a significant enhancement in the Half case; other dimension parameters

FIGURE 13: FEM results of the Standard case: SPL comparison of two cells with same hole area ratio, $a=60\mu\text{m}$ 4 holes & $a=14.5\mu\text{m}$ 68 holes (FBW: 3-dB fractional bandwidth, SPL-BWP: SPL-bandwidth product).FIGURE 14: FEM results of the Half case: SPL comparison of two cells with same hole area ratio, $a=30\mu\text{m}$ 4 holes & $a=7.25\mu\text{m}$ 68 holes (FBW: 3-dB fractional bandwidth, SPL-BWP: SPL-bandwidth product).

of this 68-hole cell are the same as the Half case in Table 2. As shown in Figure 14, the 4-hole cell still performs better than the 68-hole one, which means Helmholtz resonant effect still has a great influence for the performance improvement of the 4-hole unsealed Helmholtz structural CMUT cells in the Half case, although the characteristic of two resonant peaks is not obvious.

4.3. Range of Effectiveness for Analytical Model. From discussion above, when the $h/2\sigma_{visc}$ ratio decreases, or the hole number increases under same hole area ratio, the Helmholtz resonant effect gets weaker and even disappears. For our analytical model, the existence of Helmholtz resonant effect is a basic assumption. In Figure 11, when choosing the cavity height h , the condition $h \geq 4\sigma_{visc}$ is an FEM empirical

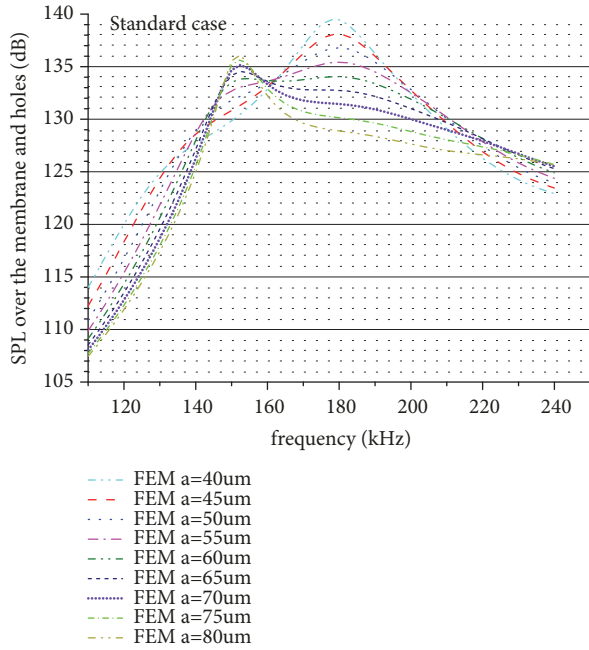


FIGURE 15: FEM results of the Standard case: sound pressure level (SPL) over the membrane and holes (dB), hole radius changes from $40 \mu\text{m}$ to $80 \mu\text{m}$ with $5 \mu\text{m}$ step size.

value that the Helmholtz resonant effect is strong enough to benefit the bandwidth of the CMUT device. Our analytical model is effective under these situations where the Helmholtz resonant effect is strong. For smaller $h/2\sigma_{visc}$ ratio, the Helmholtz resonant effect tends to disappear, and our analytical model loses efficacy. Also, for 4-hole cells in Figures 13 and 14, the Helmholtz resonant effect is strong and our analytical model is effective. For 68-holes cells, the analytical model loses efficacy. In the future work, the research attempt is to investigate the effective range of our analytical model.

4.4. The “Best” Hole Radius for Bandwidth Enhancement. From Tables 3 and 4, we can see, when f_h is close to f_p , the unsealed Helmholtz structural CMUT achieves a significant output pressure bandwidth performance enhancement. We can see a tendency that when $f_h = f_p$, the improvement should achieve the “best”. We use $5 \mu\text{m}$ step size to simulate Standard case in Figure 8 with hole radius changes from $40 \mu\text{m}$ to $80 \mu\text{m}$; the results of SPL over the membrane and holes are shown below. As Figure 15 shows, the $a=55 \mu\text{m}$, $a=60 \mu\text{m}$, and $a=65 \mu\text{m}$ cells have larger 3-dB bandwidth than other dimensions. The 3-dB fractional bandwidth are 29.4%, 35.7%, and 29.7% for $a=55 \mu\text{m}$, $60 \mu\text{m}$, and $65 \mu\text{m}$, respectively. The calculated a_{ini} which let $f_h = f_p$ is $55 \mu\text{m}$; however, its fractional bandwidth enhancement is not the “best” one. For the “best” fractional bandwidth enhancement with $a=60 \mu\text{m}$, as we described above, the f_h is close to f_p . Up to now, we cannot give a quantitative analysis for how close are the f_h and f_p for the “best” bandwidth performance enhancement. This still needs to be further investigated.

5. Conclusions

In this paper, we present the air-coupled unsealed Helmholtz structural CMUTs which utilize both Helmholtz resonant effect and squeeze film effect to enhance the device’s output pressure bandwidth performance in transmit mode. We have developed an analytical model to explain the vibration coupling between the vibration of membrane and the vibration of air pistons in the holes, which is the basic working mechanism of the Helmholtz structural CMUTs. In order to validate the analytical model, we use FEM model to simulate three cases of the 4-hole unsealed Helmholtz structural CMUT cells. From the FEM results, for the Double case, the two resonant peaks in the frequency response clearly show the vibration coupling working mechanism of the Helmholtz structural CMUT cell. For an unsealed Helmholtz structural CMUT cell with various hole radii, compared with the conventional sealed one, the improvements of 3-dB fractional SPL bandwidth and SPL-bandwidth product are around 35 times in the Standard case and 17 times in the Half case, which are achieved with the hole radius which let f_h being close to f_p . Compared with FEM results, within reasonable deviations, the analytical model can predict the characteristics such as $|U|$, SPL and f_+ and f_- of the unsealed Helmholtz structural CMUTs. In the design phase of Helmholtz structural CMUTs, this analytical model can help to initially select the cell dimensions with output pressure bandwidth performance enhancement, thus simplifying the design process and shortening the design period. The smaller $h/2\sigma_{visc}$ ratio or the more holes under the same hole area ratio, the weaker the peak majorly contributed by air pistons, which means the weaker Helmholtz resonant effect. Our analytical model loses efficacy when the Helmholtz effect tends to disappear, and the exact effective range of our analytical model still needs to be further investigated. In summary, the air-coupled 4-hole Helmholtz structural CMUT cell, which is designed based on the vibration coupling mechanism, can greatly enhance the output pressure bandwidth and keep the output pressure at a reasonable level. The analytical model can simplify the design process of this kind of CMUTs.

Data Availability

The data used to support the findings of this study are included within the article.

Conflicts of Interest

The authors declare that there are no conflicts of interest regarding the publication of this paper.

Acknowledgments

Small part of this initial work was presented (but not published) as a poster at MDDBS-BHE 2017: The 11th IEEE-EMBS International Summer School and Symposium on Medical Devices and Biosensors. This work was supported by the Science and Technology Development Fund of Macau (FDCT) under 093/2015/A3, 088/2016/A2, the University of

Macau under Grants MYRG2018-00146-AMSV, MYRG2016-00157-AMSV, MYRG2015-00178-AMSV, the Nature Science Research Project of Lingnan Normal University under Grant ZL1901, and Science and Technology Research Project of Zhanjiang City under Grant 2018B01003.

References

- [1] I. Ladabaum, X. Jin, H. T. Soh, A. Atalar, and B. T. Khuri-Yakub, "Surface micromachined capacitive ultrasonic transducers," *IEEE Transactions on Ultrasonics, Ferroelectrics and Frequency Control*, vol. 45, no. 3, pp. 678–690, 1998.
- [2] A. Caronti, G. Caliano, R. Carotenuto et al., "Capacitive micro-machined ultrasonic transducer (CMUT) arrays for medical imaging," *Microelectronics Journal*, vol. 37, no. 8, pp. 770–777, 2006.
- [3] O. Oralkan, A. S. Ergun, C.-H. Cheng et al., "Volumetric ultrasound imaging using 2-D CMUT arrays," *IEEE Transactions on Ultrasonics Ferroelectrics & Frequency Control*, vol. 50, no. 11, pp. 1581–1594, 2003.
- [4] S. Takahashi and H. Ohigashi, "Ultrasonic imaging using air-coupled P(VDF/TrFE) transducers at 2 MHz," *Ultrasonics*, vol. 49, no. 4–5, pp. 495–498, 2009.
- [5] K.-N. Huang and Y.-P. Huang, "Multiple-frequency ultrasonic distance measurement using direct digital frequency synthesizers," *Sensors and Actuators A: Physical*, vol. 149, no. 1, pp. 42–50, 2009.
- [6] K. Lindström, L. Mauritzson, G. Benoni, P. Svedman, and S. Willner, "Application of air-borne ultrasound to biomedical measurements," *Medical and Biological Engineering and Computing*, vol. 20, no. 3, pp. 393–400, 1982.
- [7] M. Kupnik, A. Schroder, and M. Groschl, "PS-16 adaptive asymmetric double-path ultrasonic transit-time gas flowmeter," in *Proceedings of the IEEE International Ultrasonics Symposium (IUS '06)*, pp. 2429–2432, Vancouver, BC, Canada, October 2006.
- [8] W. Manthey, N. Kroemer, and V. Magori, "Ultrasonic transducers and transducer arrays for applications in air," *Measurement Science and Technology*, vol. 3, no. 3, pp. 249–261, 1992.
- [9] M. Kupnik, M.-C. Ho, S. Vaithilingam, and B. T. Khuri-Yakub, "CMUTs for air coupled ultrasound with improved bandwidth," in *Proceedings of the IEEE International Ultrasonics Symposium (IUS '11)*, pp. 592–595, Orlando, Fla, USA, October 2011.
- [10] S. Hansen, A. Turo, F. Degertekin, and B. Khuri-Yakub, "Characterization of capacitive micromachined ultrasonic transducers in air using optical measurements," in *Proceedings of the IEEE International Ultrasonics Symposium (IUS '00)*, pp. 947–950, San Juan, Puerto Rico, USA, October 2000.
- [11] N. Apte, K. K. Park, and B. T. Khuri-Yakub, "Experimental evaluation of CMUTs with vented cavities under varying pressure," in *Proceedings of the IEEE International Ultrasonics Symposium (IUS '13)*, pp. 1724–1727, Prague, Czech Republic, July 2013.
- [12] N. Apte, K. K. Park, A. Nikoozadeh, and B. T. Khuri-Yakub, "Bandwidth and sensitivity optimization in CMUTs for airborne applications," in *Proceedings of the IEEE International Ultrasonics Symposium (IUS '14)*, pp. 166–169, Chicago, Ill, USA, September 2014.
- [13] N. Apte, K. K. Park, A. Nikoozadeh, and B. T. Khuri-Yakub, "Effect of fluid losses and acoustic resonances in CMUTs with vented cavities," in *Proceedings of the 18th International Conference on Solid-State Sensors, Actuators and Microsystems (Transducers 2015)*, pp. 682–685, Anchorage, Alaska, USA, June 2015.
- [14] L. E. Kinsler, A. R. Frey, A. B. Coppens, and J. V. Sanders, *Fundamentals of Acoustics*, John Wiley & Sons, Inc., 1999.
- [15] A. Octavio Manzanares and F. Montero De Espinosa, "Air-coupled MUMPs capacitive micromachined ultrasonic transducers with resonant cavities," *Ultrasonics*, vol. 52, no. 4, pp. 482–489, 2012.
- [16] O. Christensen and B. B. Vistisenm, "Simple model for low-frequency guitar function," *The Journal of the Acoustical Society of America*, vol. 68, no. 3, pp. 758–766, 1980.
- [17] V. Dickason, *Loudspeaker Design Cookbook*, Audio Amateur Pubns, 7th edition, 2005.
- [18] W. Zhang, H. Zhang, S. Jin, and Z. Zeng, "A two-dimensional CMUT linear array for underwater applications: directivity analysis and design optimization," *Journal of Sensors*, vol. 2016, Article ID 5298197, 8 pages, 2016.
- [19] U. Ingard, "On the theory and design of acoustic resonators," *The Journal of the Acoustical Society of America*, vol. 25, no. 6, pp. 1037–1061, 1953.
- [20] N. Apte, *Capacitive micromachined ultrasonic transducers with vented cavities [Ph.D. thesis]*, Stanford University, 2015.
- [21] A. Unlugedik, A. S. Tasdelen, A. Atalar, and H. Koymen, "Designing transmitting CMUT cells for airborne applications," *IEEE Transactions on Ultrasonics Ferroelectrics & Frequency Control*, vol. 61, no. 11, pp. 1899–1910, 2014.
- [22] H. K. Oguz, S. Olcum, M. N. Şenlik, V. Taş, A. Atalar, and H. Köymen, "Nonlinear modeling of an immersed transmitting capacitive micromachined ultrasonic transducer for harmonic balance analysis," *IEEE Transactions on Ultrasonics, Ferroelectrics and Frequency Control*, vol. 57, no. 2, pp. 438–447, 2010.
- [23] R. Pratap, S. Mohite, and A. K. Pandey, "Squeeze film effects in MEMS devices," *Journal of the Indian Institute of Science*, vol. 87, no. 1, pp. 75–94, 2007.
- [24] U. Ingard, *Notes on Acoustics (Physics)*, Infinity Science Press, 2008.
- [25] H. K. Oguz, A. Atalar, and H. Köymen, "Equivalent circuit-based analysis of CMUT cell dynamics in arrays," *IEEE Transactions on Ultrasonics, Ferroelectrics and Frequency Control*, vol. 60, no. 5, pp. 1016–1024, 2013.
- [26] COMSOL 5.2a, "Acoustic module users guide_thermoviscous acoustics interfaces".
- [27] Y. Yu, S. H. Pun, P. U. Mak et al., "Design of a collapse-mode CMUT with an embossed membrane for improving output pressure," *IEEE Transactions on Ultrasonics Ferroelectrics & Frequency Control*, vol. 63, no. 6, pp. 854–863, 2016.
- [28] "Axisymmetric condenser microphone," in COMSOL application gallery, <https://www.comsol.nl/model/axisymmetric-condenser-microphone-12377>.
- [29] COMSOL 5.2a, "Acoustics model library manual, piezoacoustic transducer".
- [30] D. T. Blackstock, *Fundamentals of Physical Acoustics*, John Wiley and Sons, 2000.
- [31] K. K. Park and B. T. Khuri-Yakub, "3-D airborne ultrasound synthetic aperture imaging based on capacitive micromachined ultrasonic transducers," *Ultrasonics*, vol. 53, no. 7, pp. 1355–1362, 2013.
- [32] M. Ho, M. Kupnik, K. K. Park, and B. T. Khuri-Yakub, "Long-term measurement results of pre-charged CMUTs with zero external bias operation," in *Proceedings of the IEEE International*

Ultrasonics Symposium (IUS '12), pp. 89–92, Dresden, Germany, October 2012.

- [33] S. Olcum, M. N. Senlik, and A. Atalar, "Optimization of the gain-bandwidth product of capacitive micromachined ultrasonic transducers," *IEEE Transactions on Ultrasonics, Ferroelectrics and Frequency Control*, vol. 52, no. 12, pp. 2211–2219, 2005.
- [34] <https://www.mathworks.cn/help/ident/ref/goodnessoffit.html>.

